ACS APPLIED MATERIALS & INTERFACES

www.acsami.org

Research Article

Patternable Mesoporous Thin Film Quantum Materials via Block Copolymer Self-Assembly: An Emergent Technology?

Fei Yu,[▽] R. Paxton Thedford,[▽] Konrad R. Hedderick, Guillaume Freychet, Mikhail Zhernenkov, Lara A. Estroff, Katja C. Nowack, Sol M. Gruner, and Ulrich B. Wiesner*

Cite This: *ACS Appl. Mater. Interfaces* 2021, 13, 34732–34741

Read Online

ACCESS | Metrics & More | Article Recommendations | Supporting Information

ABSTRACT: Recent developments in quantum materials hold promise for revolutionizing energy and information technologies. The use of soft matter self-assembly, for example, by employing block copolymers (BCPs) as structure directing or templating agents, offers facile pathways toward quantum metamaterials with highly tunable mesostructures via scalable solution processing. Here, we report the preparation of patternable mesoporous niobium carbonitride-type thin film superconductors through spin-coating of a hybrid solution containing an amphiphilic BCP swollen by niobia sol precursors and subsequent thermal processing in combination with photolithography. Spin-coated as-made BCP-niobia hybrid thin films on silicon substrates after optional photolithographic definition are heated in air to produce a porous oxide, and subsequently converted in a multistep process to carbonitrides via treatment with high temperatures in reactive gases including ammonia. Grazing incidence small-angle X-ray scattering suggests the presence of ordered mesostructures in as-made BCP-niobia films without further annealing, consistent with a distorted alternating gyroid morphology that is retained upon thermal treatments. Wide-angle X-ray scattering confirms the synthesis of phase-pure niobium carbonitride nanocrystals with rock-salt lattices within the mesoscale networks. Electrical transport measurements of unpatterned thin films show initial exponential rise in resistivity characteristic of thermal activation in granular systems down to 12.8 K, at which point resistivity drops to zero into a superconducting state. Magnetoresistance measurements determine the superconducting upper critical field to be over 16 T, demonstrating material quality on par with niobium carbonitrides obtained from traditional solid-state synthesis methods. We discuss how such cost-effective and scalable solution-based quantum materials fabrication approaches may be integrated into existing microelectronics processing, promising the emergence of a technology with tremendous academic and industrial potential by combining the capabilities of soft matter self-assembly with quantum materials.

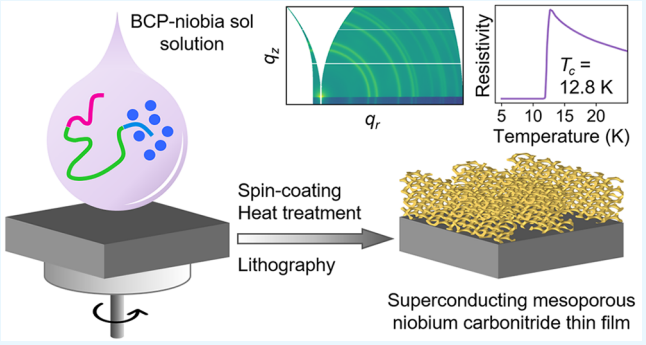

KEYWORDS: *Block Copolymer, Superconductor, Thin Film, Niobium Carbonitride, Lithography, Quantum Metamaterials*

INTRODUCTION

Nanomaterials derived from block copolymer (BCP) self-assembly are prized for their unique structures and properties, such as highly tunable morphology and periodicity, diverse form factors, large surface area porosity, biocompatibility, and so forth. They have found use in wide-ranging applications in areas including photonics,[1] separation, and purification,[2,3] and energy conversion and storage,[4,5] among others. In particular, due to their periodic self-organization on the mesoscale with lattice constants typically of order tens of nanometers, use of BCPs as self-assembling lithographic masks or templates in nanofabrication has been a highly researched area for several decades.[6,7] BCPs have been shown as capable of defining 2D and 3D periodic structures in relevant organic and inorganic materials through the process of structure direction using solution-based approaches like solvent evaporation induced self-assembly.[8,9] Numerous materials classes including transition metal oxides and nitrides, nonoxide ceramics, metals, and semiconductors have been architecturally defined on the nanoscale by BCP self-assembly in this way through methods amenable to traditional semiconductor manufacturing.[10−19]

Beyond mature silicon-based technologies, there is accelerating progress of investigations into quantum materials toward novel devices, for example, for quantum computing applications.[20] In quantum materials, including superconductors, topological insulators, quantum spin liquids or spin ices, quantum-mechanical effects fundamentally alter macroscopic

Received: May 16, 2021
Accepted: July 2, 2021
Published: July 19, 2021

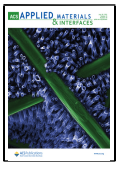

https://doi.org/10.1021/acsami.1c09085
ACS Appl. Mater. Interfaces 2021, 13, 34732–34741

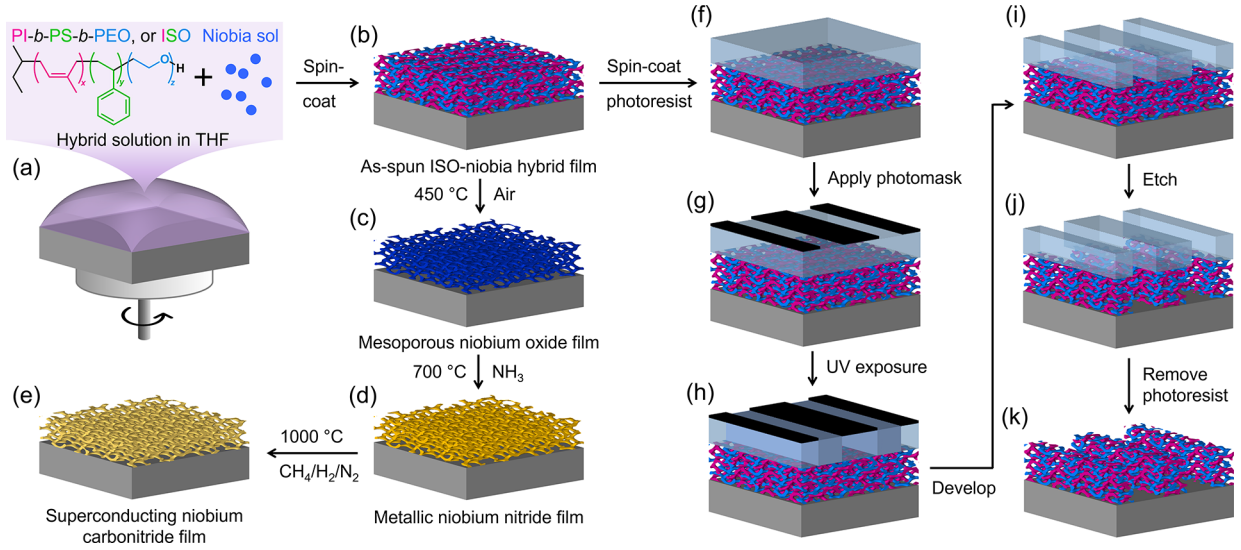

Figure 1. Schematic of solution-based fabrication processes. (a) Triblock terpolymer ISO and precursor niobia sol hybrid solution in THF is spin-coated on a silicon substrate. The sol preferentially mixes with the hydrophilic PEO block: both are depicted in false-coloring as blue. (b) As-spun ISO-niobia hybrid thin film with microphase segregated domains rendered with corresponding colors. The matrix domain of PS block is rendered transparent for illustration only; at this stage, the thin film is not porous. (c) Mesoporous niobium oxide thin film after heating in air at 450 °C. (d) Metallic niobium nitride thin film after treatment in ammonia (NH_3) at 700 °C. (e) Superconducting niobium carbonitride-type thin film after final treatment in carburizing gas ($CH_4/H_2/N_2$) at 1000 °C. (f–k) Photolithography route to prepare patterned thin films that can be further processed along (c–e).

properties.[21] BCPs have begun making inroads into such areas, demonstrating the convergence of soft matter self-assembly science and hard condensed matter physics, for example, in the form of mesostructured superconductors synthesized through structure direction or templating strategies.[22−24] These studies have shown how BCP nano/mesostructure definition can lead to emergent quantum metamaterials properties via modification of fundamental, quantum-level material characteristics. For example, when indium metal, a type-I superconductor, was confined to the minority networks of a BCP self-assembly directed double gyroid, the nanoscale confinement and periodic mesostructure led to pinning of magnetic vortices on the order of the double gyroid lattice size, resulting in macroscopic type-II superconductor behavior.[23] Furthermore, when superconducting niobium nitride-type materials were structure directed by BCPs into four different mesostructures without substantial variation of the X-ray diffraction-measured atomic lattice parameters they displayed a mesostructure-dependent transition temperature (T_c), that is, a typical fingerprint of metamaterial behavior.[24] Finally, the use of polymer solution based techniques represents a departure from the stringent conditions, for example, employing high vacuum, under which quantum materials are typically fabricated.[25] In contrast, facile and cost-effective polymer solution-based routes to quantum materials, such as spin-coating, blading, or 3D printing, promise access to a plethora of form factors not easily achievable via techniques like molecular beam epitaxy (MBE) or pulsed laser deposition (PLD).[26] It is the combination of self-assembly based control of nano/mesoscale structure and order with solution processing, which defines the scientific as well as technological interest in the emergent area of BCP-derived quantum materials.

To date, however, the investigation of BCP-based synthetic routes to such materials has been largely confined to the bulk regime.[22−24] In order to be integrated into microelectronics processing and demonstrate accessible routes toward real devices, it is desirable to create thin film analogs of such BCP-derived quantum materials. This study reports the fabrication of BCP self-assembly directed mesoporous niobium carbonitride (NbCN)-type superconducting thin film structures on silicon substrates, using a combination of spin-coating, thermal processing, and lithography. Notably, the solution-based approach leads to material properties on par with niobium carbonitrides obtained from traditional solid-state synthesis methods. We finally discuss how the demonstrated route to patternable, mesoporous superconducting thin films may become a cost-effective, highly scalable approach that could be fully integrated into existing semiconductor processing technologies toward device fabrication. As such, this work may help open pathways toward soft matter self-assembly based quantum material research with exceptional academic and industrial promise.

RESULTS AND DISCUSSION

The general solution-based fabrication route toward NbCN-type thin films on silicon substrates is depicted in Figure 1 and is based upon past efforts to synthesize similar materials in the bulk (see Experimental Section).[22,24] The structure-directing BCP used in the study is an amphiphilic triblock terpolymer poly(isoprene-*b*-styrene-*b*-ethylene oxide) (PI-*b*-PS-*b*-PEO, referred to as ISO hereafter), synthesized by sequential anionic polymerization according to a method detailed elsewhere.[27] The total number-average molar mass of ISO is 67.7 kg/mol with a polydispersity index of 1.10. The mass fractions of PI, PS, and PEO blocks were determined by ^{1}H nuclear magnetic resonance spectroscopy as 26.0%, 65.3%, and 8.7%, respectively, a composition targeted for achieving the alternating gyroid (G^A) morphology.[28] The inorganic niobia sol precursor is prepared in tetrahydrofuran (THF) from the hydrolytic condensation of niobium(V) ethoxide under acidic conditions. Upon mixing the sol solution with a solution of ISO in THF and subsequent spin-coating and solvent evaporation induced

https://doi.org/10.1021/acsami.1c09085
ACS Appl. Mater. Interfaces 2021, 13, 34732−34741

self-assembly (Figure 1a,b), the niobia sol particles selectively mix with the hydrophilic PEO block of the ISO to form a nanostructured composite thin film.[22]

After spin-coating on a silicon substrate, the ISO-niobia hybrid thin films consist of two interpenetrating minority networks formed by the PI block (Figure 1b, magenta) and the PEO block swollen with niobia (Figure 1b, blue) embedded in a PS matrix (Figure 1b, left transparent). At this stage, as-made composite films are readily patternable through conventional photolithographic means as schematically depicted in Figure 1f–k. Using wet or dry etching techniques (Figure 5 and Experimental Section) the ISO-niobia thin films can thus be defined into arbitrary areas and shapes, which are subsequently transformed into superconducting material through further thermal processing. Without any further efforts on post-deposition annealing such as low temperature thermal or solvent vapor annealing (SVA), the hybrid films are treated in air at elevated temperatures up to 450 °C to further condense the niobia and remove the structure directing ISO. Fourier-transform infrared spectroscopy (FTIR) results of as-made and heat-treated samples show the expected disappearance of vibrational bands characteristic of organic components, while thermogravimetric analysis (TGA) documents the associated sample weight loss (Figure S1). The resulting niobium oxide thin films (Figure 1c) show locally ordered mesoporous structures, as evidenced by scanning electron microscopy (SEM, Figure 2a). X-ray scattering experiments suggest the

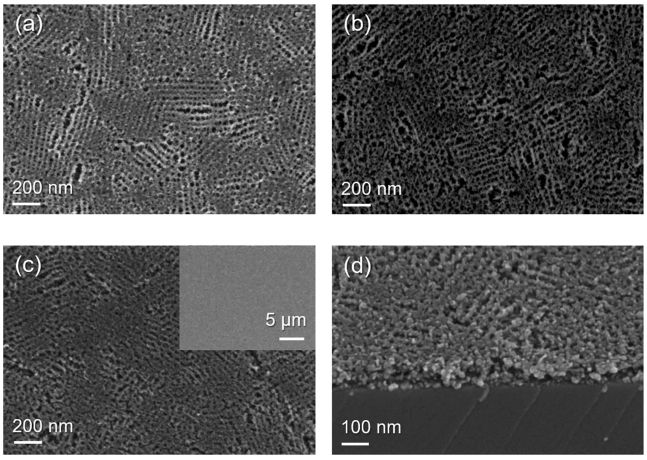

Figure 2. Scanning electron microscopy (SEM) images of thin films at different processing stages and length scales. Plan views of (a) the niobium oxide film; (b) the niobium nitride film; (c) the niobium carbonitride film (inset at low-magnification demonstrates uniformity across macroscopic length scales). (d) A 45° cross-sectional view of the niobium carbonitride film displaying the film edge on the cleaved silicon substrate (lower darker part).

morphology of these films is consistent with a deformed G^A structure (vide infra; Supplemental Note 1 and Figure S2), in which the niobia in the original hybrid film is retained as a single inorganic minority network replicating the PEO plus inorganic domain after the decomposition of polymeric components. To render the thin films electrically conducting, a subsequent nitridation in ammonia (NH_3) is carried out at 700 °C converting the mesoporous oxide into a niobium nitride (NbN, Figure 1d), albeit with some oxygen (and vacancies) likely remaining as discussed in detail in a previous study.[24] The mesostructure appears largely unchanged through this process with a slight coarsening of the nodes in the network (Figure 2b).

Finally, heating the NbN thin films to 1000 °C in a mixture of methane (CH_4), hydrogen (H_2), and nitrogen (N_2), known as carburizing gas ($CH_4/H_2/N_2$) yields a superconducting niobium carbonitride (NbCN)-type material (Figure 1e) without substantial further growth in crystallite size, as demonstrated earlier.[24] The overall mesoporous structure is retained, albeit with additional coalescence of struts discernible in images of the top surface (Figure 2c). With the simple spin-coating technique, a uniform thin film with arbitrary lateral dimensions can be fabricated without major macroscopic defects such as large cracks (see low-magnification inset of Figure 2c and Figure S3). The thickness of the final niobium carbonitride film is approximately 100 nm (Figure 2d); film thickness is expected to be adjustable through varying concentrations of the starting hybrid solution or spinning speeds during spin-coating. Pore sizes as estimated from SEM results are of order 20 to 30 nm.

To obtain structural information about the thin films beyond a local scale probed by electron microscopy, X-ray scattering experiments were performed at the National Synchrotron Light Source II (NSLS-II) Soft Matter Interfaces (SMI) beamline[32] in a grazing incidence geometry. In previous work, an amphiphilic triblock terpolymer with similar block fractions swollen by niobia sol or other additives was shown to self-assemble into the G^A mesophase,[22,28,33] with {110} planes of the G^A parallel to the substrate in the case of thin films.[34] The SEM images in Figure 2 display a morphology in which seemingly parallel struts lie at the surface with a set of thinner struts crossing underneath at 90° (see Supplemental Note 1). Such observations agree with previous results of G^A thin films with the same orientation, but with possible nascent epitaxial growth into the cylindrical phase.[35] As seen in grazing incidence small-angle X-ray scattering (GISAXS), the primary peak, which would correspond to the (110) plane given a G^A morphology, persists in samples at all stages (Figure 3a,b). Detailed analysis of a GISAXS scattering pattern (Supplemental Note 1) taken from an as-made ISO-niobia sol composite thin film is consistent with a deformed G^A structure with {110} planes parallel to the substrate, which mainly shrinks in the film's normal direction during processing (Figures S2 and S4). This deformation at the unit cell level due to anisotropic forces has been detailed previously in other self-assembling gyroidal systems.[19,36] It is worth reemphasizing that no efforts were made to improve long-range order of the films via postspin-coating annealing. The degree of mesostructural order as reflected by SEM and GISAXS experiments is the result of the very rapid evaporation of THF during spin-coating and likely represents a structure away from equilibrium. Another notable feature of the GISAXS profiles in Figure 3b is that peak shifting to larger in-plane scattering vector q_y as a result of in-plane shrinkage upon thermal processing is much less pronounced as compared to the bulk.[22] This is likely leading to anisotropic stresses caused by pinning of the films to the supporting substrate during shrinkage. Indeed, a limited amount of network breakage via disconnection of neighboring struts is seen in SEM images of thin film top surfaces (Figure 2 and Figure S5) upon treatment at elevated temperatures, consistent with this picture.

Overcoming a threshold in atomic crystal quality (for example, eliminating oxygen or vacancies) is essential for superconductivity in NbCN-type thin films at low temper-

https://doi.org/10.1021/acsami.1c09085
ACS Appl. Mater. Interfaces 2021, 13, 34732−34741

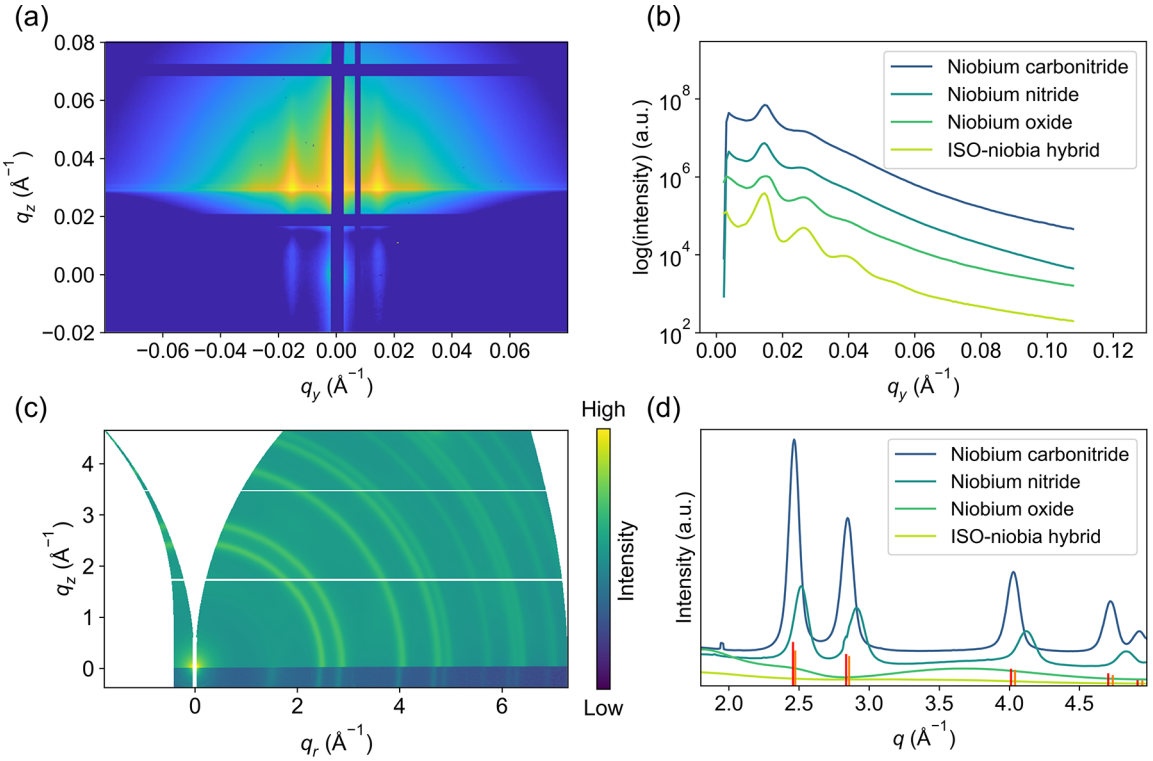

Figure 3. Grazing incidence small-angle X-ray scattering (GISAXS) and wide-angle X-ray scattering (GIWAXS) profiles of thin films at different processing stages. The scattering vector q is defined as $4\pi \sin\theta/\lambda$, where 2θ is the scattering angle and λ is the wavelength of X-rays. The subscripts r, y, and z denote the q component within the plane along the in-plane y direction perpendicular to the X-ray beam and along the out-of-plane z direction, respectively. (a) The 2D GISAXS pattern of carbonitride film after heat treatment to 1000 °C. (b) Line cuts through the Yoneda band[29] of GISAXS patterns for different films as a function of processing step, as indicated. (c) The 2D GIWAXS pattern of carbonitride film after heat treatment to 1000 °C. (d) Azimuthal integration of GIWAXS intensities for different films as a function of processing step, as indicated. Orange and red ticks show expected peak positions and their relative intensities of NbN from the powder diffraction file (PDF) #03-065-0436 and of NbC from PDF #03-065-8781, respectively.[30,31]

atures; this is revealed by grazing incidence wide-angle X-ray scattering (GIWAXS, Figure 3c,d) results. Scattering peaks in the form of multiple concentric rings appear in the 2D pattern, suggesting small, randomly oriented atomically crystalline domains (Figure 3c). This powderlike pattern is expected for nanocrystals forming in a cubic (that is, isotropic) mesostructured gyroid network as nucleation takes place homogeneously throughout the structure and no preference exists for crystallographic orientation. Consistent with earlier results,[22,24] NbN (or oxynitride) crystallizes first from an amorphous niobium oxide after nitridation at 700 °C in NH_3 (Figure 3d). Compared with peak positions expected for cubic rock-salt NbN (lattice parameter 4.39 Å), the phase-pure crystals have a smaller lattice parameter of 4.32 Å, likely due to remaining oxygen and vacancy defects present in the structure (i.e., $NbN_xO_y[]_{1-x-y}$, where [] denotes vacancies).[24] Final treatment in $CH_4/H_2/N_2$ at an even higher temperature of 1000 °C introduces carbon content and increases the lattice size to 4.41 Å, between that of rock-salt NbN and NbC (lattice parameter of 4.43 Å; Figure S6). Along with an increased lattice parameter, coherently scattering domain sizes calculated using the Scherrer equation grew from 4.3 nm in NbN-type films to 5.8 nm in NbCN films. In general, various NbCN films treated under the same conditions were found to have coherent scattering domain sizes ranging from 4.8 to 5.8 nm. Consistent with earlier results, the high-temperature processing does not lead to substantial crystal growth, which is responsible for the good structure preservation at the mesoscale across the various processing steps.[24]

For comparison, dense carbonitride thin films were synthesized via spin-coating of a pure niobia sol solution (that is, without ISO) and heat treatment under identical conditions (denoted as the "dense film" hereafter). GIWAXS results show such dense films have a coherent crystallite size on the lower end of the range seen in the porous NbCN films, that is, 5.2 nm, according to Scherrer analysis. Overall, consistent with observations and discussions in our previous bulk materials study,[22,24] we hypothesize that the mesoporous structures induced by the coassembly with ISO facilitates the diffusion of reactive gas species to and from the material during high-temperature heat treatments and promotes solid-state reactions with low tendency for recrystallization, leading to the very slow grain growth observed.[24] This hypothesis is consistent with conventional wisdom, that bulk diffusion significantly contributes to domain growth only at $T > 0.5\ T_m$ (T_m is the material's melting point) from which for these materials one would not expect bulk crystal growth from temperature alone until about 1150 °C.

Superconductivity in mesoporous NbCN thin films was probed via DC transport measurements (Figure 4), utilizing a van der Pauw geometry with four chromium/gold metal contacts deposited on the film perimeter via thermal evaporation through a shadow mask (see Experimental Section, Figure S3). The resistivity, ρ, of the mesoporous NbCN film (Figure 4a) was measured to be 6.91 $\mu\Omega$·cm at 300

https://doi.org/10.1021/acsami.1c09085
ACS Appl. Mater. Interfaces 2021, 13, 34732−34741

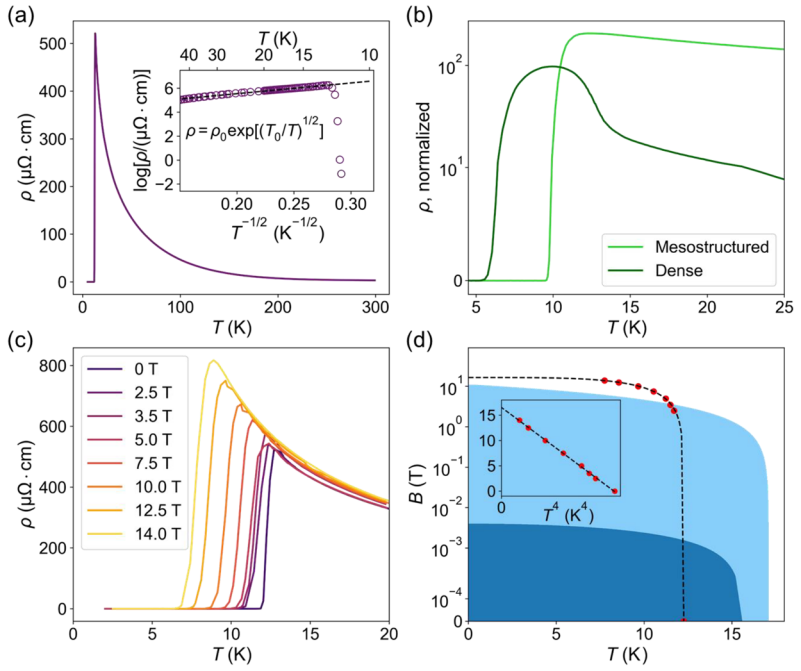

Figure 4. Electrical transport measurements of mesoporous superconducting niobium carbonitride thin films on silicon substrates heat treated in $CH_4/H_2/N_2$ at a temperature of 1000 °C. Measurements were performed using the van der Pauw method. (a) Plot of resistivity (ρ) as a function of temperature (T) at zero field. The inset shows the plot of the logarithm of ρ as a function of $T^{-1/2}$. The linear behavior before the superconducting transition can be fitted with an Arrhenius-like exponential dependence of the form $\rho = \rho_0 \exp\left[\left(\frac{T_0}{T}\right)^{1/2}\right]$ with $\rho_0 = 43\ \mu\Omega$·cm and $T_0 = 80$ K. (b) Plot of ρ (normalized with respect to 300 K) as a function of T for mesostructured and dense niobium carbonitride thin films. (c) Plot of ρ of the film in (a) as a function of T at varying field strengths. (d) Plot of upper critical field (B_{c2}) as a function of T, together with the depiction of the phase diagram of niobium (carbo)nitride superconductors. The relationship between critical field (B_c) and T is $B_c = B_c(T=0)\left[1 - \left(\frac{T}{T_c}\right)^{\alpha}\right]$, where T_c is the critical temperature, and α is an empirical fitting parameter. Red points are our experimental B_{c2} values at corresponding T determined as when ρ decreases to half the peak value before the superconducting transition. The data points are fitted with $\alpha = 4$, shown as the dashed line. The dark blue region represents the behavior of superconducting niobium nitride with a lower critical field (B_{c1}) of 4.0 mT and a T_c of 15.2 K from ref 37 with the boundary fitted with $\alpha = 2$. The light blue region represents the mixed state of normal and superconducting niobium carbonitride with B_{c2} of 11 T and T_c of 16.7 K from ref 38 with the boundary fitted with $\alpha = 1$.[39] The inset shows the linear fit of our experimental B_{c2} values when the horizontal axis represents T raised to the power of 4.

K, comparable to that of the dense film, 5.65 $\mu\Omega$·cm. It should be noted that the porosity of the film was not considered for the calculation of resistivity, so the value is likely an overestimation (see Supplemental Note 2). During zero-field cooling (ZFC) of the carbonitride, however, a precipitous rise in the resistivity was observed down to the transition temperature (T_c) of 12.8 K with a relatively low value of $\rho_{300K}/\rho_{12.8K} = 0.0065$. At 12.8 K, a sharp decrease to zero resistivity occurred indicating the transition into a superconducting state. This temperature is below the T_c of ∼17.3 K observed in sputtered NbCN films.[40] The decrease in T_c could be due to differences in the carbon/nitrogen ratio in the mesoporous films as compared to controlled sputter deposition or to the retention of oxygen or vacancies in the material, as the NbCN synthesized here was converted from a parent oxide rather than grown in an oxygen-free environment. It is also notable that the T_c of the mesoporous sample under ZFC is slightly higher than that of the comparative dense films (Figure 4b). This result is further confirmation that the induced porosity and very high surface area in the ISO templated films facilitate material conversions during processing and improve final superconductor quality, possibly through increased reactivity with gaseous species as a result of significantly shortened diffusion distances during annealing enabled by the nanostructure.

The exponential rise in resistivity with decreasing temperature down to T_c is reminiscent of the behavior reported in granular superconducting samples[41] and has been observed previously in nanocrystalline NbN films.[42−46] In these materials, the finite charging energy associated with individual grains can lead to thermally activated, Arrhenius-like dependence of conductivity on temperature as is evidenced in Figure 4a (inset).[41] An additional contribution to the increased resistivity upon cooling may be increased grain boundary scattering of electrons in the highly granular NbCN thin films.[44] In the case of the mesoporous NbCN thin films of the present work, disorder and granularity in the material arise from both the small crystallite size as well as the nanoscale mesostructural network features. It is notable that these two parameters are of the same order: the coherent scattering domain size in the NbCN is measured to be 5.8 nm, while the thinnest points of the struts comprising the mesoscale network are ∼10 nm or less (Figure 2, Figure S5). For nanocrystalline NbCN materials structure directed by BCPs, these two parameters are separately tunable through high-temperature processing or selection of the BCP templating agent molar mass, respectively. This may become an important future tool

https://doi.org/10.1021/acsami.1c09085
ACS Appl. Mater. Interfaces 2021, 13, 34732−34741

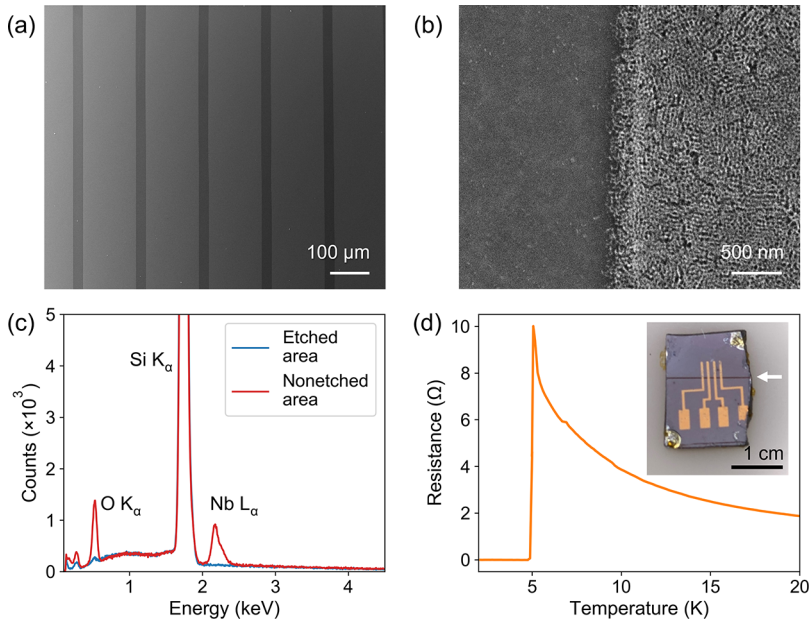

Figure 5. Lithographic patterning of spin-coated thin films on silicon substrates. (a) Plan-view SEM image of niobium carbonitride thin film patterned through photolithography with 25 μm wide strips etched away shown in dark. (b) Higher-magnification SEM image of the patterned film showing the edge along with details of the self-assembled mesostructure. (c) Energy-dispersive X-ray spectroscopy (EDS) spectra of areas of plain film (that is, nonetched area) and etched film after 10 min CF_4 plasma etching. The blue curve for etched area is obscured where it overlaps with and lies under the red one for nonetched area. (d) Plot of resistance versus temperature as obtained from an individual patterned 400 μm wide strip thin film area. Inset shows a single lithographically patterned niobium carbonitride strip (400 μm wide) visible to the naked eye (white arrow) with four colinear metal contacts across the strip used for the transport measurements. Note that the niobium carbonitride strip shows up as a darker line against the background in this image captured by an optical microscope, as opposed to the darker area that is etched away in (a), which is captured by SEM.

for elucidation of the impact of physical confinement on the same order as the average grain size in granular metals and superconductors.

Upon transitioning into the superconducting state at 12.8 K, resistivity is entirely lost. Magnetoresistance measurements of the NbCN thin film (Figure 4c) show that a high upper critical field (B_{c2}) is maintained in the mesoporous films, estimated to be over 16 T (Figure 4d). This is higher than the B_{c2} of ∼11 T observed previously in bulk NbCN matieral,[38,39] which further speaks to the relatively high quality materials properties that can be achieved via scalable solution based synthesis techniques. Comparing the upper critical field of the mesoporous NbCN at varying temperatures against the superconducting phase diagram of niobium nitride (Figure 4d) accentuates this.

It is relevant to point out that nanocrystallinity and mesoscale structuring has been observed to increase the critical field strength in superconductors due to the effect on materials structure at the scale of the coherence length.[23,47,48] However, despite having a slightly larger coherent scattering domain size, the estimated critical field in the mesoporous film is notably higher than that seen in the comparative dense film created via a sol−gel route without the use of BCP self-assembly (Figure S7). While materials stoichiometry could be at play, the high lattice constant present in the dense film indicates a low level of oxygen and vacancy content. Thus, the mesostructure itself may play an important role in critical field enhancement via the contribution of surface superconductivity or the increased granularity associated with the interpenetrating strut networks.

As a proof-of-concept, we defined microscopic patterns via photolithography on spin-coated BCP self-assembly directed thin films to illustrate compatibility of our solution-based synthesis approaches to mesoporous superconducting samples with typical semiconductor nanofabrication processing (Figure 1f–k). First, a photoresist is applied on the ISO-niobia hybrid thin films that are pretreated at 300 °C to minimize swelling or dissolution of the film by photoresist solution but without complete removal of the ISO template (see Experimental Section). After exposure through a mask and development, 25 μm wide strips of photoresist layers are removed. Pattern transfers are achieved by a combination of wet etching using buffered oxide etchant (BOE, to remove niobia) and dry etching using oxygen plasma (to remove polymeric components). The observed clear and sharp patterns demonstrate the viability for spin-coated ISO-niobia thin films to be incorporated into standard microelectronic processing with additional self-assembled 3D features at the mesoscale (Figure 5a,b).

A separate pattern was transferred from a shadow mask using CF_4 plasma etching. Transfer fidelity is much higher for the ISO-niobia hybrid thin film before any high-temperature heat treatments, whereas the features become smeared when using the mesoporous niobium oxide films (Figures S8 and S9). Porosity in the mesostructured film likely contributes to poor pattern transfer by allowing plasma to infiltrate void spaces thereby causing undesirable etching of regions of niobium oxide covered/shielded by the mask. This is also likely one of the causes behind the slanted edge seen in Figure 5b. Results suggest that the dry etching of thin films with internal nanostructures derived from structure directing agents such as BCPs should proceed before the introduction of porosity in order to maximize directional anisotropy. For our spin-coated films, both CF_4 plasma etching or a combination of wet and

https://doi.org/10.1021/acsami.1c09085
ACS Appl. Mater. Interfaces 2021, 13, 34732−34741

dry etching could completely remove the ISO-niobia hybrid materials, as evidenced by the disappearance of the Nb L_α peak in energy-dispersive X-ray spectroscopy (EDS) experiments (Figure 5c). Films patterned via plasma etching into 400 μm wide strips (Figure 5d, inset, white arrow) were found to retain superconductivity at low temperature but with a transition reduced to 5 K (Figure 5d). This shift could be due to chemical inhomogeneity across the surface of mesoporous thin films, which would create multiple percolating superconducting paths of varying composition and transition temperature.

CONCLUSIONS

In summary, we reported the preparation of superconducting mesoporous niobium carbonitride-type thin films on silicon substrates derived from BCP self-assembly with niobia precursors using standard polymer solution-based processing in combination with thermal treatments at elevated temperatures under different gas environments. In more detail, the material fabrication route involved spin-coating of ISO terpolymer-niobia sol hybrid solutions and a series of heat treatments in air, ammonia, and carburizing gas at temperatures up to 1000 °C to result in controllable mesoporosity, nanocrystallinity, and superconducting thin film properties. Specific steps to perfect the BCP self-assembly derived structure after spin-coating, for example, by means of low-temperature thermal or SVA, were not taken but could be added in future protocols. Finally, in proof-of-principle experiments, thin films were shown to be amenable to lithographic patterning through common dry or wet etching techniques, all compatible with regular semiconductor processing. While the relatively high temperatures required to achieve self-assembly directed mesostructure conversion into superconducting materials at first may seem to pose a roadblock to further technology developments, it is perhaps instructive to note that this hurdle may be overcome by the use of transient laser annealing methods.[49] Such methods represent a proven technology currently used in large scale semiconductor manufacturing to eliminate high-temperature furnace treatments. Furthermore, they have previously been demonstrated for the conversion of BCP self-assembly directed hybrid thin films into mesoporous templates as well as for their conformal backfilling with crystalline silicon (cSi) using transient laser annealing processes reaching temperatures above the cSi melting temperature (that is, over 1400 °C).[14,17,19] We therefore anticipate a clear path toward the development of solution-based approaches to thin film technologies at the intersection between soft matter self-assembly and quantum materials with tremendous academic as well as industrial potential. In particular, the diversity of BCP self-assembly and tunability of structural parameters, for example, via BCP composition and molar mass, provide unprecedented opportunities for the discovery of fundamentally new physics as well as device functionality for potential applications ranging from information technology all the way to energy conversion and storage and sensing.[50]

EXPERIMENTAL SECTION

Preparation of Niobium Carbonitride Thin Films on Silicon Substrates. Unless otherwise stated, all chemicals were purchased from Millipore-Sigma. Silicon substrates were obtained from Pure Wafer (resistivity 0.01−0.02 Ω·cm, doped with boron). Pure gases and gas blends used for thermal film treatments were obtained from Airgas.

The protocol for the sequential anionic polymerization of the triblock terpolymer ISO can be found in prior published work.[27] A combination of proton nuclear magnetic resonance (^{1}H NMR) spectroscopy and gel permeation chromatography (GPC) was used to determine total number-average polymer molar mass (M_n) of 67.7 kg/mol, polydispersity index (PDI) of 1.10, and block weight fractions for PI, PS, and PEO blocks of 26.0%, 65.3%, and 8.7%, respectively.

The preparation of niobia sol and ISO-niobia hybrid solutions is also detailed in a previous publication and was used with slight modifications.[22] First, 0.50 g of ISO was dissolved in 7.00 g of anhydrous (99.9%) tetrahydrofuran (THF). In a separate vial for the sol stock solution, 0.96 mL of niobium(V) ethoxide (99.999%, Alfa Aesar) was injected to a mixture of 0.56 mL of 37 wt % HCl solution and 0.90 mL of anhydrous THF under vigorous stirring. After 5 min, another 4.5 mL anhydrous THF was injected to the vial to slow down the hydrolytic condensation. After 2 min of additional stirring, 1.40 g of sol stock solution was added to the ISO solution. The hybrid solution was stirred for 20 h before spin-coating at 2000 rpm for 45 s on a ∼1 × 1 cm^2 silicon substrate. For Fourier-transform infrared spectroscopy (FTIR) and thermogravimetric analysis (TGA) characterizations, the hybrid solution was prepared from 0.050 g of ISO mixed with 0.268 mL (for FTIR) or 0.147 mL (for TGA) niobia sol stock solution in 1.0 mL THF. The hybrid solution was poured into a Teflon beaker (inner diameter ∼1 cm) and heated at 40 °C under a glass dome to evaporate the solvent THF, resulting in a bulk film.

To further condense the niobia sol, the ISO-niobia hybrid thin films were heat treated at 130 °C in air for about 3 h at which stage cross-sectional SEM images showed films to be ∼650 nm thick. The films were calcined in a tube furnace under static ambient air to remove the templating ISO and to obtain mesoporous niobium oxide films. The heating ramp rate was set at 1 °C/min to 450 °C with a dwell time of 3 h at this temperature. Through this process step, the thickness of the niobium oxide films dramatically reduced to ∼110 nm, again determined from cross-sectional SEM images. The nitridation of the niobium oxide films was performed in a quartz tube furnace using electronic grade ammonia (99.9995% purity) at a flow rate of 8 L/h. The heating protocol used included a ramp rate of 5 °C/min to 700 °C with a 9 h dwell time at that temperature. For comparative studies between mesostructured and dense thin films, the dwell time in this nitridation step was 3 h. Superconducting niobium carbonitride films were derived by treating the niobium nitride films under carburizing gas ($CH_4/H_2/N_2$, 16/4/80 by mole fraction) at a flow rate of 8 L/h, heated at 5 °C/min to 1000 °C with a 3 h dwell time. The thickness of the final films after this stage was observed to be ∼100 nm from cross-sectional SEM images, that is, only slightly reduced from that of the nitride films.

Patterning of Niobium Carbonitride Thin Films. Shadow masks were made by cutting fused silica wafers from University Wafer (thickness 180 μm) using a CO_2 laser cutter (VersaLaser VLS3.50). The laser spot size was 25.4 μm operated at 1000 dpi with 1.5% power and 2% speed set in the controlling software. The widths of strips cut out ranged from 25 to 800 μm.

To etch the thin films into a strip with defined widths via only dry etching, the shadow mask was placed onto the film and CF_4 plasma was applied for 10 min (30 sccm at 40 mTorr, 150 W power) using an Oxford PlasmaLab 80+ etcher.

To pattern thin films using photolithography, ISO-niobia hybrid thin films were first heated at 300 °C for 3 h to further condense the niobia and partially pyrolyze the ISO. After treating films with hexamethyldisilazane primer, S1813 resist was spin-coated on the films at 3000 rpm for 30 s (acceleration 10 000 rpm/s). The photoresist was then exposed to ultraviolet light (365 nm) for 3 min in vacuum contact mode in an ABM contact aligner. After developing in Microposit MF-321 Developer for 90 s, the photoresist layer had a trench depth of ∼1.6 μm (measured by a Tencor P7 Profilometer). Thin films were then etched by two cycles of 1 min descum process in the Oxford PlasmaLab 80+ etcher (50 sccm oxygen at 20 mTorr, 50 W power) and a 20 min dip in buffered oxide etchant (BOE, 6:1 concentration). The patterned thin films were finally heat treated

https://doi.org/10.1021/acsami.1c09085
ACS Appl. Mater. Interfaces 2021, 13, 34732−34741

using the same protocol as detailed in the previous section in order to convert them into niobium carbonitride.

Characterization. *Fourier-Transform Infrared Spectroscopy (FTIR).* FTIR experiment was conducted on Bruker Vertex 80V system in vacuum using the attenuated total reflectance (ATR) configuration. The bulk films of the ISO-niobia hybrid and the niobium oxide after calcination at 450 °C were ground to powder using a mortar and pestle. Spectra were collected using a deuterated triglycine sulfate (DTGS) detector.

Thermogravimetric Analysis (TGA). TGA data was obtained on a TA Instruments Q500 system using bulk films of the ISO-niobia hybrid. A monolithic piece of the ISO-niobia hybrid was heated to 600 °C at a rate of 10 °C/min in air while measuring the retained sample mass in order to determine the mass loss.

Scanning Electron Microscopy (SEM). SEM images were captured with an in-beam secondary electron (SE) or regular SE detector using a Tescan Mira3 field emission scanning electron microscope (FESEM) operating at 5 kV accelerating voltage or with an inlens EsB detector using a Zeiss GeminiSEM 500 operating at 2 kV accelerating voltage. Samples were coated with gold−palladium prior to imaging (optional).

Grazing Incidence X-ray Scattering. Grazing incidence X-ray scattering experiments were performed at the National Synchrotron Light Source II (NSLS-II) Soft Matter Interfaces (SMI) beamline with an X-ray energy of 14.0 keV and incident angle of 0.10°. Grazing incidence small-angle X-ray scattering (GISAXS) patterns were recorded on a Pilatus3 1 M pixel array detector with a sample-to-detector distance (SDD) of 4.97 m. GISAXS data were processed using the MATLAB-based software GIXSGUI (version 1.7.1)[51] to plot the 2D pattern and produce a line-cut profile through the Yoneda band.[29] Grazing incidence wide-angle X-ray scattering (GIWAXS) patterns were recorded on a Pilatus3 300 K-W pixel array detector positioned at 274 mm from the samples. The detector was rotated along a goniometer arc to capture multiple frames with the scattering angle ranging from −3.5° to 62°. Individual GIWAXS frames were stitched and processed using customized python codes at SMI[52] to plot the 2D pattern in reciprocal space and to azimuthally integrate the intensity. Scherrer analysis was performed using JADE software on the (111), (200), (220), and (311) peaks (the four peaks with smallest q shown in Figure 3d). A pseudo-Voigt profile was used for peak fitting. The coherently scattering domain sizes τ calculated from the Scherrer equation $\tau = \frac{K\lambda}{\beta \cos\theta}$ were averaged to obtain the result. The shape factor K was 0.93, while β was the respective peak broadening at half-maximum.

Low-Temperature Transport Property Measurements. Heat-treated NbCN thin films on silicon substrates were cleaved with a diamond scribe to remove ∼1 mm from the perimeter of the roughly square samples on every side. This step was taken to prevent inhomogeneous edge material from the spin coating process contributing to transport measurements. Metal contacts of ∼10 nm of chromium immediately followed by ∼30 nm of gold were then deposited directly onto the films through a custom cut shadow mask using a Varian bell jar thermal evaporator. The configuration of metal contacts defined in this way are shown in Figure S3 (van der Pauw configuration for regular films) and in Figure 5d (inset, a colinear configuration for patterned strips).

Transport properties of samples were measured using a Quantum Design Physical Properties Measurement System (PPMS) equipped with a helium reliquifier and 14 T magnet. Samples were mounted onto a standard PPMS resistivity puck using Lakeshore cryogenic varnish and deposited chromium/gold contacts were wirebonded to metal puck contact pads with aluminum wire using a Westbond model 7400E wedge−wedge ultrasonic/thermosonic wire bonder. In a typical measurement, the external field of the instrument was ramped to the specified field, for example, 2.5 T, at a rate of 10 mT/s and held at that value. An excitation current of 100 μA was then applied, and the resistance value measured while heating or cooling the sample through the measurement range, that is, 2−20 K, at a rate of 2 K/min. At each point of the resistivity assessment, the average of five measurements was reported as the value of resistance with an observed relative error at least 2 orders of magnitude lower than the reported value. For van der Pauw configurations, this was repeated for both the vertical and horizontal configurations to obtain the final resistivity value. For patterned films (Figure 5), the transport measurement shown in panel d was repeated several times without substantial variation between measurements.

■ ASSOCIATED CONTENT

Supporting Information

The Supporting Information is available free of charge at https://pubs.acs.org/doi/10.1021/acsami.1c09085.

Supplemental notes on the structural analysis from GISAXS results and the resistivity of porous films with internal mesostructures; supplemental figures of FTIR and TGA results, additional GISAXS/GIWAXS data, photos of samples, structural illustrations, SEM images, and low-temperature transport property measurement data (PDF)

■ AUTHOR INFORMATION

Corresponding Author

Ulrich B. Wiesner − *Department of Materials Science and Engineering, Cornell University, Ithaca, New York 14853, United States;* orcid.org/0000-0001-6934-3755; Email: ubw1@cornell.edu

Authors

Fei Yu − *Department of Materials Science and Engineering and Department of Chemistry and Chemical Biology, Cornell University, Ithaca, New York 14853, United States;* orcid.org/0000-0002-8191-8096

R. Paxton Thedford − *Department of Materials Science and Engineering and Robert Frederick Smith School of Chemical and Biomolecular Engineering, Cornell University, Ithaca, New York 14853, United States;* orcid.org/0000-0003-0811-227X

Konrad R. Hedderick − *Department of Materials Science and Engineering, Cornell University, Ithaca, New York 14853, United States*

Guillaume Freychet − *National Synchrotron Light Source-II, Brookhaven National Laboratory, Upton, New York 11973, United States*

Mikhail Zhernenkov − *National Synchrotron Light Source-II, Brookhaven National Laboratory, Upton, New York 11973, United States;* orcid.org/0000-0003-3604-0672

Lara A. Estroff − *Department of Materials Science and Engineering, Cornell University, Ithaca, New York 14853, United States; Kavli Institute at Cornell for Nanoscale Science, Ithaca, New York 14853, United States;* orcid.org/0000-0002-7658-1265

Katja C. Nowack − *Department of Physics, Cornell University, Ithaca, New York 14853, United States*

Sol M. Gruner − *Kavli Institute at Cornell for Nanoscale Science, Ithaca, New York 14853, United States; Department of Physics, Cornell University, Ithaca, New York 14853, United States*

Complete contact information is available at: https://pubs.acs.org/10.1021/acsami.1c09085

Author Contributions

[▽]F.Y. and R.P.T. contributed equally.

Notes

The authors declare no competing financial interest.

■ ACKNOWLEDGMENTS

Funding support from the U.S. Department of Energy (DOE), Office of Science (Basic Energy Sciences, award DE-SC0010560) is gratefully acknowledged. We made use of shared facilities at the Cornell Center for Materials Research, which is supported through the National Science Foundation (NSF) MRSEC program (DMR-1719875), and at the Cornell NanoScale Facility, a member of the National Nanotechnology Coordinated Infrastructure (NNCI), which is supported by the NSF (NNCI-2025233). This research used Soft Matter Interfaces (SMI, 12-ID) beamline of the National Synchrotron Light Source II, a U.S. DOE Office of Science User Facility operated for the DOE Office of Science by Brookhaven National Laboratory under Contract No. DE-SC0012704. Proton nuclear magnetic resonance (^{1}H NMR) spectroscopy was performed at the Cornell University NMR facility, which is supported in part by the NSF through MRI award (CHE-1531632). R.P.T. was supported by the NSF Graduate Research Fellowship Program under Grant DGE-1650441. We thank Peter A. Beaucage for helpful discussions and Anthony M. Condo Jr. for TGA experiments.

■ REFERENCES

(1) Urbas, A.; Sharp, R.; Fink, Y.; Thomas, E. L.; Xenidou, M.; Fetters, L. J. Tunable Block Copolymer/Homopolymer Photonic Crystals. *Adv. Mater.* **2000**, *12* (11), 812−814.

(2) Peinemann, K.-V.; Abetz, V.; Simon, P. F. W. Asymmetric Superstructure Formed in a Block Copolymer via Phase Separation. *Nat. Mater.* **2007**, *6* (12), 992−996.

(3) Dorin, R. M.; Phillip, W. A.; Sai, H.; Werner, J.; Elimelech, M.; Wiesner, U. Designing Block Copolymer Architectures for Targeted Membrane Performance. *Polymer* **2014**, *55* (1), 347−353.

(4) Werner, J. G.; Rodríguez-Calero, G. G.; Abruña, H. D.; Wiesner, U. Block Copolymer Derived 3-D Interpenetrating Multifunctional Gyroidal Nanohybrids for Electrical Energy Storage. *Energy Environ. Sci.* **2018**, *11* (5), 1261−1270.

(5) Li, C.; Li, Q.; Kaneti, Y. V.; Hou, D.; Yamauchi, Y.; Mai, Y. Self-Assembly of Block Copolymers towards Mesoporous Materials for Energy Storage and Conversion Systems. *Chem. Soc. Rev.* **2020**, *49* (14), 4681−4736.

(6) Park, M.; Harrison, C.; Chaikin, P. M.; Register, R. A.; Adamson, D. H. Block Copolymer Lithography: Periodic Arrays of ~10^{11} Holes in 1 Square Centimeter. *Science* **1997**, *276* (5317), 1401−1404.

(7) Bates, C. M.; Maher, M. J.; Janes, D. W.; Ellison, C. J.; Willson, C. G. Block Copolymer Lithography. *Macromolecules* **2014**, *47* (1), 2−12.

(8) Orilall, M. C.; Wiesner, U. Block Copolymer Based Composition and Morphology Control in Nanostructured Hybrid Materials for Energy Conversion and Storage: Solar Cells, Batteries, and Fuel Cells. *Chem. Soc. Rev.* **2011**, *40* (2), 520−535.

(9) Hoheisel, T. N.; Hur, K.; Wiesner, U. B. Block Copolymer-Nanoparticle Hybrid Self-Assembly. *Prog. Polym. Sci.* **2015**, *40*, 3−32.

(10) Kamperman, M.; Garcia, C. B. W.; Du, P.; Ow, H.; Wiesner, U. Ordered Mesoporous Ceramics Stable up to 1500 °C from Diblock Copolymer Mesophases. *J. Am. Chem. Soc.* **2004**, *126* (45), 14708−14709.

(11) Malenfant, P. R. L.; Wan, J.; Taylor, S. T.; Manoharan, M. Self-Assembly of an Organic−Inorganic Block Copolymer for Nano-Ordered Ceramics. *Nat. Nanotechnol.* **2007**, *2* (1), 43−46.

(12) Warren, S. C.; Messina, L. C.; Slaughter, L. S.; Kamperman, M.; Zhou, Q.; Gruner, S. M.; DiSalvo, F. J.; Wiesner, U. Ordered Mesoporous Materials from Metal Nanoparticle-Block Copolymer Self-Assembly. *Science* **2008**, *320* (5884), 1748−1752.

(13) Lee, J.; Orilall, M. C.; Warren, S. C.; Kamperman, M.; DiSalvo, F. J.; Wiesner, U. Direct Access to Thermally Stable and Highly Crystalline Mesoporous Transition-Metal Oxides with Uniform Pores. *Nat. Mater.* **2008**, *7* (3), 222−228.

(14) Arora, H.; Du, P.; Tan, K. W.; Hyun, J. K.; Grazul, J.; Xin, H. L.; Muller, D. A.; Thompson, M. O.; Wiesner, U. Block Copolymer Self-Assembly−Directed Single-Crystal Homo- and Heteroepitaxial Nanostructures. *Science* **2010**, *330* (6001), 214−219.

(15) Kim, E.; Vaynzof, Y.; Sepe, A.; Guldin, S.; Scherer, M.; Cunha, P.; Roth, S. V.; Steiner, U. Gyroid-Structured 3D ZnO Networks Made by Atomic Layer Deposition. *Adv. Funct. Mater.* **2014**, *24* (6), 863−872.

(16) Robbins, S. W.; Sai, H.; DiSalvo, F. J.; Gruner, S. M.; Wiesner, U. Monolithic Gyroidal Mesoporous Mixed Titanium−Niobium Nitrides. *ACS Nano* **2014**, *8* (8), 8217−8223.

(17) Tan, K. W.; Jung, B.; Werner, J. G.; Rhoades, E. R.; Thompson, M. O.; Wiesner, U. Transient Laser Heating Induced Hierarchical Porous Structures from Block Copolymer-Directed Self-Assembly. *Science* **2015**, *349* (6243), 54−58.

(18) Lim, H.; Kani, K.; Henzie, J.; Nagaura, T.; Nugraha, A. S.; Iqbal, M.; Ok, Y. S.; Hossain, Md. S. A.; Bando, Y.; Wu, K. C. W.; Kim, H.-J.; Rowan, A. E.; Na, J.; Yamauchi, Y. A Universal Approach for the Synthesis of Mesoporous Gold, Palladium and Platinum Films for Applications in Electrocatalysis. *Nat. Protoc.* **2020**, *15* (9), 2980−3008.

(19) Yu, F.; Zhang, Q.; Thedford, R. P.; Singer, A.; Smilgies, D.-M.; Thompson, M. O.; Wiesner, U. B. Block Copolymer Self-Assembly-Directed and Transient Laser Heating-Enabled Nanostructures toward Phononic and Photonic Quantum Materials. *ACS Nano* **2020**, *14* (9), 11273−11282.

(20) Basov, D. N.; Averitt, R. D.; Hsieh, D. Towards Properties on Demand in Quantum Materials. *Nat. Mater.* **2017**, *16* (11), 1077−1088.

(21) Keimer, B.; Moore, J. E. The Physics of Quantum Materials. *Nat. Phys.* **2017**, *13* (11), 1045−1055.

(22) Robbins, S. W.; Beaucage, P. A.; Sai, H.; Tan, K. W.; Werner, J. G.; Sethna, J. P.; DiSalvo, F. J.; Gruner, S. M.; Van Dover, R. B.; Wiesner, U. Block Copolymer Self-Assembly−Directed Synthesis of Mesoporous Gyroidal Superconductors. *Sci. Adv.* **2016**, *2* (1), No. e1501119.

(23) Thedford, R. P.; Beaucage, P. A.; Susca, E. M.; Chao, C. A.; Nowack, K. C.; Van Dover, R. B.; Gruner, S. M.; Wiesner, U. Superconducting Quantum Metamaterials from High Pressure Melt Infiltration of Metals into Block Copolymer Double Gyroid Derived Ceramic Templates. *Adv. Funct. Mater.* **2021**, *31* (23), 2100469.

(24) Beaucage, P. A.; Van Dover, R. B.; DiSalvo, F. J.; Gruner, S. M.; Wiesner, U. B. Superconducting Quantum Metamaterials from Convergence of Soft and Hard Condensed Matter Science. *Adv. Mater.* **2021**, *33*, 2006975.

(25) Samarth, N. Quantum Materials Discovery from a Synthesis Perspective. *Nat. Mater.* **2017**, *16* (11), 1068−1076.

(26) Diao, Y.; Shaw, L.; Bao, Z.; Mannsfeld, S. C. B. Morphology Control Strategies for Solution-Processed Organic Semiconductor Thin Films. *Energy Environ. Sci.* **2014**, *7* (7), 2145−2159.

(27) Bailey, T. S.; Pham, H. D.; Bates, F. S. Morphological Behavior Bridging the Symmetric AB and ABC States in the Poly(Styrene-*b*-Isoprene-*b*-Ethylene Oxide) Triblock Copolymer System. *Macromolecules* **2001**, *34* (20), 6994−7008.

(28) Werner, J. G.; Hoheisel, T. N.; Wiesner, U. Synthesis and Characterization of Gyroidal Mesoporous Carbons and Carbon Monoliths with Tunable Ultralarge Pore Size. *ACS Nano* **2014**, *8* (1), 731−743.

(29) Yoneda, Y. Anomalous Surface Reflection of X Rays. *Phys. Rev.* **1963**, *131* (5), 2010−2013.

(30) Lengauer, W.; Ettmayer, P. Preparation and Properties of Compact Cubic δ-NbN1-x. *Monatsh. Chem.* **1986**, *117* (3), 275−286.

(31) Rudy, E.; Benesovsky, F.; Sedlatschek, K. Untersuchungen im System Niob-Molybdän-Kohlenstoff. *Monatsh. Chem.* **1961**, *92* (4), 841−855.

https://doi.org/10.1021/acsami.1c09085
ACS Appl. Mater. Interfaces 2021, 13, 34732−34741

(32) Zhernenkov, M.; Canestrari, N.; Chubar, O.; DiMasi, E. Soft Matter Interfaces Beamline at NSLS-II: Geometrical Ray-Tracing vs. Wavefront Propagation Simulations. *Proc. SPIE* 2014, 9209, 92090G.
(33) Li, Z.; Hur, K.; Sai, H.; Higuchi, T.; Takahara, A.; Jinnai, H.; Gruner, S. M.; Wiesner, U. Linking Experiment and Theory for Three-Dimensional Networked Binary Metal Nanoparticle-Triblock Terpolymer Superstructures. *Nat. Commun.* **2014**, *5*, 3247.
(34) Zhang, Q.; Matsuoka, F.; Suh, H. S.; Beaucage, P. A.; Xiong, S.; Smilgies, D.-M.; Tan, K. W.; Werner, J. G.; Nealey, P. F.; Wiesner, U. B. Pathways to Mesoporous Resin/Carbon Thin Films with Alternating Gyroid Morphology. *ACS Nano* **2018**, *12* (1), 347−358.
(35) Guliyeva, A.; Vayer, M.; Warmont, F.; Takano, A.; Matsushita, Y.; Sinturel, C. Transition Pathway between Gyroid and Cylindrical Morphology in Linear Triblock Terpolymer Thin Films. *Macromolecules* **2019**, *52* (17), 6641−6648.
(36) Feng, X.; Burke, C. J.; Zhuo, M.; Guo, H.; Yang, K.; Reddy, A.; Prasad, I.; Ho, R.-M.; Avgeropoulos, A.; Grason, G. M.; Thomas, E. L. Seeing Mesoatomic Distortions in Soft-Matter Crystals of a Double-Gyroid Block Copolymer. *Nature* **2019**, *575* (7781), 175−179.
(37) Mathur, M. P.; Deis, D. W.; Gavaler, J. R. Lower Critical Field Measurements in NbN Bulk and Thin Films. *J. Appl. Phys.* **1972**, *43* (7), 3158−3161.
(38) Raine, M. J.; Hampshire, D. P. Characterization of the Low Temperature Superconductor Niobium Carbonitride. *IEEE Trans. Appl. Supercond.* **2011**, *21* (3), 3138−3141.
(39) Note that the value of B_{c2} of 11 T reported in ref 38 is extrapolated using data taken from multiple types of measurements of ac-susceptibility, magnetic hysteresis, and heat capacity, in addition to resistivity that is the property probed in this work.
(40) Gavaler, J. R.; Janocko, M. A.; Jones, C. K. Superconducting Properties of Niobium Carbonitride Thin Films. *Appl. Phys. Lett.* **1971**, *19* (8), 305−307.
(41) Beloborodov, I. S.; Lopatin, A. V.; Vinokur, V. M.; Efetov, K. B. Granular Electronic Systems. *Rev. Mod. Phys.* **2007**, *79* (2), 469−518.
(42) Nigro, A.; Nobile, G.; Rubino, M. G.; Vaglio, R. Electrical Resistivity of Polycrystalline Niobium Nitride Films. *Phys. Rev. B: Condens. Matter Mater. Phys.* **1988**, *37* (8), 3970−3972.
(43) Tyan, J.-H.; Lue, J. T. Grain Boundary Scattering in the Normal State Resistivity of Superconducting NbN Thin Films. *J. Appl. Phys.* **1994**, *75* (1), 325−331.
(44) Senapati, K.; Pandey, N. K.; Nagar, R.; Budhani, R. C. Normal-State Transport and Vortex Dynamics in Thin Films of Two Structural Polymorphs of Superconducting NbN. *Phys. Rev. B: Condens. Matter Mater. Phys.* **2006**, *74* (10), 104514.
(45) Sanjinés, R.; Benkahoul, M.; Sandu, C. S.; Schmid, P. E.; Lévy, F. Electronic States and Physical Properties of Hexagonal β-Nb 2N and δ'-NbN Nitrides. *Thin Solid Films* **2006**, *494* (1−2), 190−195.
(46) Kang, L.; Jin, B. B.; Liu, X. Y.; Jia, X. Q.; Chen, J.; Ji, Z. M.; Xu, W. W.; Wu, P. H.; Mi, S. B.; Pimenov, A.; Wu, Y. J.; Wang, B. G. Suppression of Superconductivity in Epitaxial NbN Ultrathin Films. *J. Appl. Phys.* **2011**, *109* (3), 033908.
(47) Bose, S.; Ayyub, P. A Review of Finite Size Effects in Quasi-Zero Dimensional Superconductors. *Rep. Prog. Phys.* **2014**, *77* (11), 116503.
(48) Taylor, D. M. J.; Al-Jawad, M.; Hampshire, D. P. A New Paradigm for Fabricating Bulk High-Field Superconductors. *Supercond. Sci. Technol.* **2008**, *21* (12), 125006.
(49) Tan, K. W.; Wiesner, U. Block Copolymer Self-Assembly Directed Hierarchically Structured Materials from Nonequilibrium Transient Laser Heating. *Macromolecules* **2019**, *52* (2), 395−409.
(50) Broholm, C.; Fisher, I.; Moore, J.; Murnane, M.; Moreo, A.; Tranquada, J.; Basov, D.; Freericks, J.; Aronson, M.; MacDonald, A.; Fradkin, E.; Yacoby, A.; Samarth, N.; Stemmer, S.; Horton, L.; Horwitz, J.; Davenport, J.; Graf, M.; Krause, J.; Pechan, M.; Perry, K.; Rhyne, J.; Schwartz, A.; Thiyagarajan, T.; Yarris, L.; Runkles, K. Basic Research Needs Workshop on Quantum Materials for Energy Relevant Technology. USDOE Office of Science, South Carolina, United States, 2016, DOI: 10.2172/1616509.
(51) Jiang, Z. GIXSGUI: A MATLAB Toolbox for Grazing-Incidence X-Ray Scattering Data Visualization and Reduction, and Indexing of Buried Three-Dimensional Periodic Nanostructured Films. *J. Appl. Crystallogr.* **2015**, *48* (3), 917−926.
(52) Pandolfi, R. J.; Allan, D. B.; Arenholz, E.; Barroso-Luque, L.; Campbell, S. I.; Caswell, T. A.; Blair, A.; De Carlo, F.; Fackler, S.; Fournier, A. P.; Freychet, G.; Fukuto, M.; Gürsoy, D.; Jiang, Z.; Krishnan, H.; Kumar, D.; Kline, R. J.; Li, R.; Liman, C.; Marchesini, S.; Mehta, A.; N'Diaye, A. T.; Parkinson, D. Y.; Parks, H.; Pellouchoud, L. A.; Perciano, T.; Ren, F.; Sahoo, S.; Strzalka, J.; Sunday, D.; Tassone, C. J.; Ushizima, D.; Venkatakrishnan, S.; Yager, K. G.; Zwart, P.; Sethian, J. A.; Hexemer, A. Xi-Cam: A Versatile Interface for Data Visualization and Analysis. *J. Synchrotron Radiat.* **2018**, *25* (4), 1261−1270.

https://doi.org/10.1021/acsami.1c09085
ACS Appl. Mater. Interfaces 2021, 13, 34732−34741